Local Observation of the Site Occupancy of Mn in a MnFePSi Compound

M. J. Neish, M. P. Oxley, J. Guo, B. C. Sales, L. J. Allen, and M. F. Chisholm

Phys. Rev. Lett. **114**, 106101 — Published 11 March 2015

DOI: 10.1103/PhysRevLett.114.106101

Local observation of the site occupancy of Mn in a MnFePSi compound

M. J. Neish,[1] M. P. Oxley,[2,3] J. Guo,[4] B. C. Sales,[2] L. J. Allen,[1] and M. F. Chisholm[2]

[1] *School of Physics, University of Melbourne, Parkville, Victoria 3010, Australia*
[2] *Materials Science and Technology Division, Oak Ridge National Laboratory, Oak Ridge, Tennessee 37831, USA*
[3] *Department of Physics and Astronomy, Vanderbilt University, Nashville, Tennessee 37212, USA*
[4] *Department of Materials Science and Engineering, University of Tennessee, Knoxville, Tennessee 37996, USA*

(Dated: February 23, 2015)

MnFePSi compounds are promising materials for magnetic refrigeration as they exhibit a giant magnetocaloric effect. From first principles calculations and experiments on bulk materials it has been proposed that this is due to the Mn and Fe atoms preferentially occupying two different sites within the atomic lattice. A recently developed technique was used to deconvolve the obscuring effects of both multiple elastic scattering and thermal diffuse scattering of the probe in an atomic resolution electron energy-loss spectroscopy investigation of an MnFePSi compound. This reveals unambiguously that the Mn atoms preferentially occupy the $3g$ site in a hexagonal crystal structure, confirming the theoretical predictions. After deconvolution the data exhibits a difference in the Fe $L_{2,3}$ ratio between the $3f$ and $3g$ sites, consistent with differences in magnetic moments calculated from first principles, which are also not observed in the raw data.

PACS numbers: 68.37.Ma, 75.30.Sg, 75.50.Bb, 79.20.Uv

Magnetocaloric materials have attracted considerable interest in recent years due to their technological applications [1–4]. In the presence of a changing external magnetic field, heat may be either absorbed or radiated from the material [3], and magnetic refrigeration based on the magnetocaloric effect (MCE) has the potential to replace vapor compression refrigeration due to its greater energy efficiency [4, 5]. In particular, Fe_2P compounds are known to display giant MCEs [5, 6], a behavior that was first observed in MnFePAs [1]. Since this discovery, efforts have been made to replace the toxic element As with ecofriendly components while maintaining a low thermal hysteresis [5]. To this end, MnFePSi compounds with a hexagonal Fe_2P-type structure have recently been found to show a giant MCE with a small hysteresis over a large temperature range [4]. Combined with a composition of abundant, nontoxic elements, this makes MnFePSi compounds promising materials for room temperature refrigeration [6, 7].

$(Mn,Fe)_{1.95}P_{1-x}Si_x$ compounds are reported to have a hexagonal Fe_2P-type structure with x varying between 0.28 and 0.64, and an orthorhombic Co_2P-type structure for $x \leq 0.24$ [7]. In both these structures, two metal sites containing an equal number of atoms are present – the tetragonally coordinated $3f$ site, here labeled Fe1, and the pyramidally coordinated $3g$ site, here labeled Fe2 [8]. By varying the Fe:Mn ratio in the compound, as well as increasing the amount of Si present, a decrease in the thermal hysteresis is observed [4]. It is believed that the site occupancy of the Fe and Mn atoms gives rise to this property. It was first inferred from Mössbauer spectroscopy in a pure MnFeP compound that Fe atoms preferentially populate the Fe1 atomic sites, and Mn atoms the Fe2 atomic sites [9], an observation that has more recently been repeated for a $Fe_{1.02}Mn_{0.98}P_{0.5}Si_{0.5}$ compound [8]. The preferential occupancy of the Fe2 sites by Mn has also been deduced by using neutron diffraction [10]. Density functional theory (DFT) calculations support this observation [4, 8, 11]. Here we will use atomic resolution elemental mapping using an atomic-scale scanning transmission electron microscopy (STEM) probe to investigate the occupancy of the Mn atoms and also Fe $L_{2,3}$ ratios at the *local* atomic level. Such column-by-column information is not obtainable from neutron diffraction. This approach is not limited to periodic structures alone and an important application of this work will be to study interfaces.

Atomic resolution elemental mapping in STEM using electron energy-loss spectroscopy (EELS) allows for the precise determination of the identity, location, and bonding of the atoms within a sample of condensed matter [12–16]. However, channeling (multiple elastic scattering) and thermal diffuse scattering of the probe are inevitably present in the elemental maps, even for quite thin specimens, and this hinders direct interpretation [17]. For quantitative experimental analysis, either simulations incorporating channeling and thermal diffuse scattering need to be carried out [17] or alternatively these effects need to be deconvolved from the data, the approach we have followed here [18]. In contrast with previous investigations of MnFePSi compounds which were only able to study a large section of the sample, in this Letter we have used STEM EELS to obtain atomic resolution chemical maps of the Mn $L_{2,3}$ and Fe $L_{2,3}$ edges of a $Mn_{0.43}Fe_{1.57}P_{0.73}Si_{0.27}$ compound. Carrying out the essential additional step of deconvolving the obfuscating multiple elastic and thermal diffuse scattering of the probe from the data then reveals unambiguously that the Mn atoms preferentially occupy the $3g$ site in a hexagonal crystal structure. The deconvolved data also exhibits

a difference in the Fe $L_{2,3}$ ratio between the $3f$ and $3g$ sites, consistent with differences in magnetic moments calculated from first principles.

Single crystals of $Mn_{0.43}Fe_{1.57}P_{0.73}Si_{0.27}$ were grown at high temperatures ($900 - 1125$ °C) using a molten tin flux [19, 20]. The Sn was decanted at 900 °C leaving small needle-shaped crystals with typical dimensions of $2 \times 0.1 \times 0.1$ mm^3, and crystallized in the hexagonal Fe_2P structure. The crystal examined was taken from a batch with an average T_c of 340 K, but the exact value is very sensitive to the precise Si content [10]. The ferromagnetic to paramagnetic transition was only weakly hysteretic, $\Delta T_c \approx 3$ K (warming versus cooling). The crystals were cooled through T_c during preparation. The environment in the microscope produces a field of about 2 T at the sample location, which is more than enough to fully magnetize the Mn and Fe spins. The compositions of the crystals were determined using energy dispersive x-ray analysis and the hexagonal structure was verified using single crystal x-ray diffraction.

STEM EELS images and a simultaneously acquired high-angle annular dark-field (HAADF) image were obtained on a Nion UltraSTEM200 fitted with a Gatan Enfinium operating at 200 kV. The $Mn_{0.43}Fe_{1.57}P_{0.73}Si_{0.27}$ specimen was aligned in the $\langle 001 \rangle$ projection. The probe convergence angle α was 30 mrad and the EELS collection angle β was 36 mrad. The inner and outer collection angles of the simultaneously acquired HAADF image were 65 mrad and 400 mrad respectively. EEL spectra were recorded from a 30×36 pixel region, corresponding to a physical area of 9.8×11.8 Å^2. The energy resolution was 0.35 eV due to the energy spread of the beam. Low-loss and core-loss spectra were acquired separately in order to maximize the core-loss signal on the spectrometer. The specimen thickness was determined to be 65 nm by fitting a modified Drude model to the low-loss spectrum [21].

Figure 1 (a) and (b) show the experimentally acquired and simulated HAADF STEM images respectively. The finite source size of the electron probe has been accounted for by convolution with a suitable function in the simulated image. Recently, it has been shown that a combination of Gaussian and Lorentzian functions is required to accurately model the source size [22–24]. We follow the approach of Xin *et al.* [25] by modeling the effective source as a Gaussian convolved with a Lorentzian. By careful comparison with the experimental data, a Gaussian with a half-width at half-maximum (HWHM) of 0.3 Å convolved with a Lorentzian with a HWHM of 0.05 Å was chosen.

STEM EELS images as a function of probe position for the Fe $L_{2,3}$ edge (edge onset: 708 eV) and Mn $L_{2,3}$ edge (edge onset: 640 eV) are shown in Figs. 1(c) and (e) respectively. The energy-loss windows over which the spectra were integrated to form the images (630-670 eV for Mn, 690-740 eV for Fe) are free of contributions from

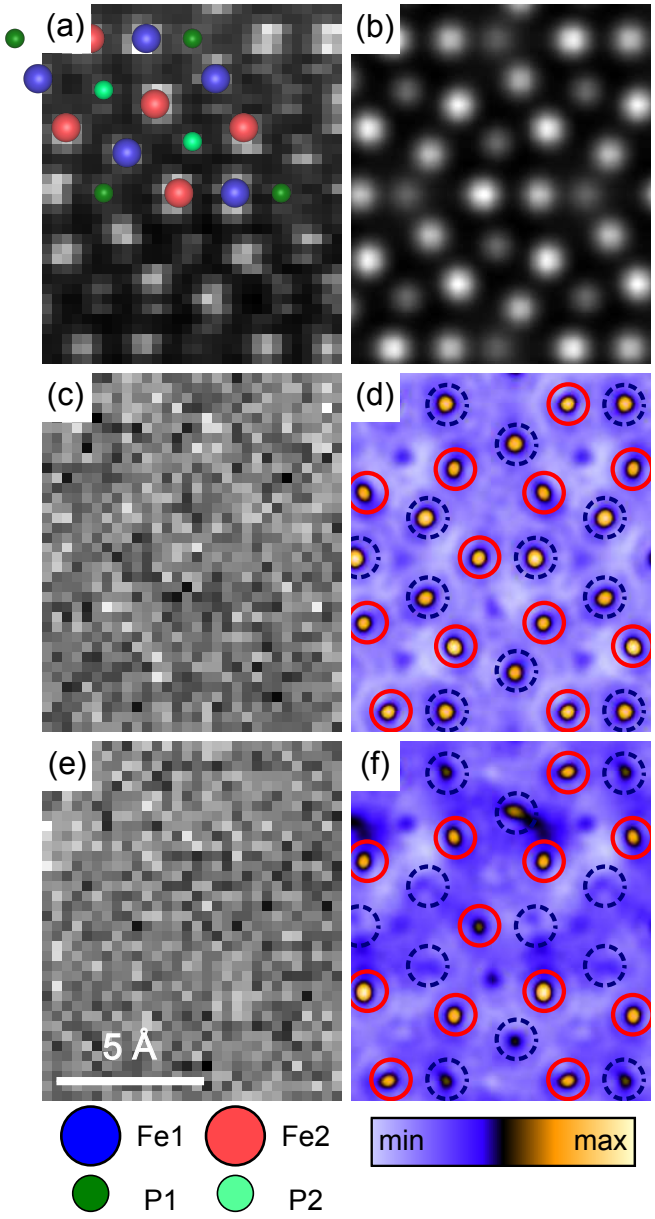

FIG. 1. (Color online) (a) Experimental atomic resolution HAADF image of $Mn_{0.43}Fe_{1.57}P_{0.73}Si_{0.27}$, with the projected atomic structure overlaid. (b) Simulated HAADF image, assuming an incoherent effective source function of a Gaussian with a HWHM of 0.3 Å convolved with a Lorentzian with a HWHM of 0.05 Å. (c) Experimental EELS map and (d) inelastic scattering potential of the Fe $L_{2,3}$ edge. (e) Experimental EELS map and (f) inelastic scattering potential of the Mn $L_{2,3}$ edge, showing a preference for Mn on the Fe2 sites. The open blue (dashed) and red (solid) circles in (d) and (f) represent the expected locations of the Fe1 and Fe2 atomic columns respectively.

the P and Si atoms within the specimen. Background subtraction was performed using the Cornell Spectrum Imager plugin for ImageJ [26]. Assuming that most of the energy loss electrons enter the detector (a point we will return to later), the recorded intensities in Figs. 1(c) and (e) can be modeled, as a function of probe position $\mathbf{R}$ and integrating up over the energy losses E in the energy-loss window, in the following form:

$$\begin{aligned} I(\mathbf{R}) &= \int I(\mathbf{R}, E) dE \\ &= \frac{4\pi m}{h^2 k} \frac{1}{A} \int_A \int_0^t \left|\psi(\mathbf{R}, \mathbf{r}_\perp, z)\right|^2 dz \int V(\mathbf{r}_\perp, E) dE d\mathbf{r}_\perp \,. \end{aligned} \tag{1}$$

The presence of the probability density of the probe $|\psi(\mathbf{R}, \mathbf{r}_\perp, z)|^2$ in this expression, where $\mathbf{r}_\perp$ is perpendicular to the optical axis with coordinate z, expresses the fact that multiple elastic scattering and thermal diffuse scattering of the probe complicate the relationship between the measured intensity $I(\mathbf{R})$ and the potential $V(\mathbf{r}_\perp, E)$ describing the energy-loss interaction (for a specific edge). It is this last quantity which is related to properties of the material and correctly reflects the stoichiometry. The quantities m and k are the relativistically corrected electron mass and wave number respectively, A is the area of the region illuminated by the probe and t is the specimen thickness.

Since Mn and Fe differ in atomic number by only one, the depth-integrated quantity $\int_0^t |\psi(\mathbf{R}, \mathbf{r}_\perp, z)|^2 dz$ is insensitive to the precise distribution of Mn and Fe atoms, as is also true for P and Si (and this has been verified in simulation). Therefore, we have assumed this quantity to be that calculated for a pure Fe_2P structure. It can be considered to be the known kernel in an integral equation for the unknown quantity $\int V(\mathbf{r}_\perp, E) dE$, which can be obtained by inversion provided that $I(\mathbf{R})$ is suitably sampled with respect to probe position. The inversion of the integral equation is accomplished using the conjugate gradients least squares (CGLS) method to iteratively solve a set of linear equations. As is often the case with inverse problems, regularization is required and this is accomplished in the CGLS method by terminating at a suitable iteration number, as described in Ref. 27. This approach also very effectively exposes the physical information that may otherwise be masked by noise, as can be seen by the application of the inversion procedure to obtain the energy integrated potentials in Figs. 1(d) and (f) from the measured data in Figs. 1(c) and (e) respectively.

While the Fe lattice is just visible in the Fe $L_{2,3}$ edge in Fig. 1(c) and not distinguishable in the Mn $L_{2,3}$ edge in Fig. 1(e), atomic columns are clearly resolved in the corresponding potentials. The open blue (dashed) and red (solid) circles in Fig. 1(d) and (f) represent the expected locations of the Fe1 and Fe2 atomic columns respectively. It can clearly be seen that both sites are occupied in the Fe $L_{2,3}$ edge, but the Fe2 site is favored for the Mn $L_{2,3}$ edge, agreeing with previous results inferred from bulk specimens and DFT simulations. We note that there is some Mn signal on Fe1 sites and on some P sites, and that these may be artifacts originating from the low signal to noise ratio in the Mn EELS map.

We note that the form of Eq. (1) assumes that all scattered energy-loss electrons are collected by the EELS detector. This requires that the EELS collection angle used is large [28]. For the EELS collection angle used here, a significant fraction of the energy-loss electrons are outside the detector, in particular those which have also been scattered to large angles via phonon excitation. The modest collection angle of 36 mrad was chosen as it gives a better energy resolution by avoiding high angle spectrometer aberrations. It has recently been proposed [29] that the effect of a finite detector size may be corrected by multiplying the experimental image with the reciprocal of an incoherent bright field (BF) image, obtained by integration of a simultaneously acquired low-loss EELS spectrum image. As a simultaneously acquired low-loss data set was not available, we simulated a BF image matching the experimental parameters, again by assuming a Fe_2P structure. Each slice in the experimental data cube was divided by the simulated BF image, correcting for the electrons scattered outside the detector, making the application of Eq. (1) more accurate. The finite source size of the incident probe was accounted for by convolving both the BF image and the kernel used in the inversion [the depth integrated wave function in Eq. (1)] with the same distribution used previously for the simulated HAADF image.

The EELS maps and inelastic scattering potentials presented in Fig. 1 were obtained by integrating over the entire energy-loss edge, including the energy-loss near-edge structure. By considering smaller energy-loss windows, we can obtain a potential for each energy loss and extract spectra similar to those traditionally obtained from the data after background subtraction. Firstly we will consider energy-loss spectra obtained from a pure experimental analysis before application of the inversion procedure. Figures 2(a) and (b) show the Fe $L_{2,3}$ edge obtained from Fe1 and Fe2 sites respectively, averaged across 10 columns. Typical individual spectra are indicated by the gray lines in each subplot. For ease of visual comparison, the averaged spectra from each site [colored lines in Fig. 2(a) and (b)] are displayed in Fig. 2(c). A slight dip can be seen in the L_3 peak at approximately 708 eV on the Fe1 sites. This analysis was then repeated for the scattering potentials obtained after inversion, using a 0.3 eV energy window (chosen to be comparable with the experimental energy resolution), the results of which are shown in Fig. 3. After performing the inversion, the dip in the L_3 peak at the Fe1 site is far more pronounced. The $L_{2,3}$ ratio is dependant on local electronic

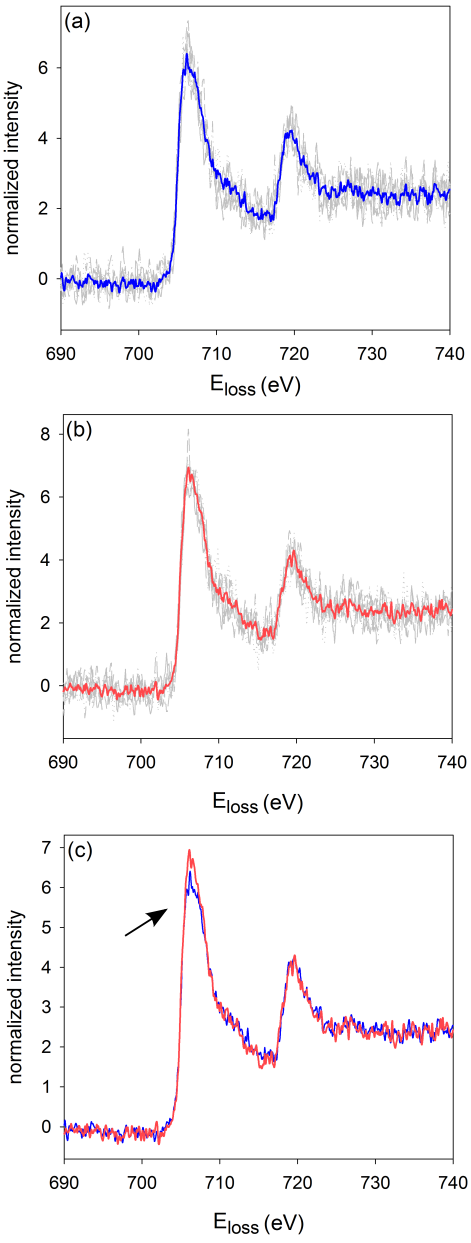

FIG. 2. (Color online) Energy-loss spectra obtained from analyzing the experimental data. (a) Fe1 $L_{2,3}$ and (b) Fe2 $L_{2,3}$ spectra averaged across 10 columns using a 3×3 pixel region around each column. The gray lines show 5 typical individual spectra. (c) Comparison between the averaged Fe1 and Fe2 $L_{2,3}$ spectra. A slight dip is seen in the L_3 peak for the Fe1 sites, as indicated by the arrow.

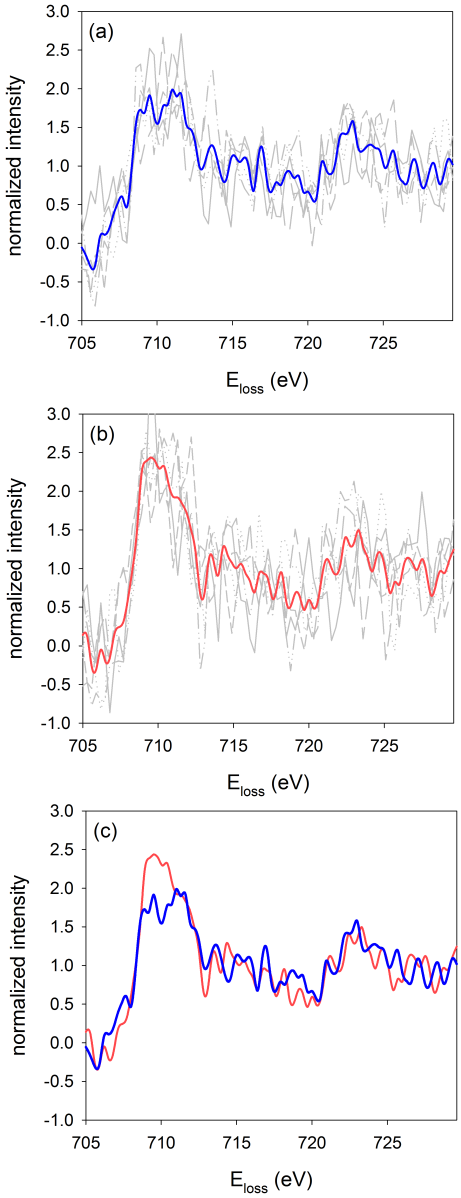

FIG. 3. (Color online) Energy-loss spectra obtained from the inelastic scattering potentials. (a) Fe1 $L_{2,3}$ and (b) Fe2 $L_{2,3}$ spectra averaged across the columns in a unit cell (colored lines). The gray lines show 5 typical individual spectra. (c) Comparison between the averaged Fe1 (blue) and Fe2 (red) $L_{2,3}$ spectra. The dip in the L_3 peak for the Fe1 sites is far more pronounced.

structure and has been shown to reflect differences in both oxidation states [30] and magnetic moments [31, 32]. DFT calculations for the pure Fe_2P substance give a magnetic moments of 1.03 μ_B and 1.91 μ_B for the Fe1 and Fe2 sites respectively [33]. The reduction in the Fe $L_{2,3}$ ratio seen in Fig. 3(c) is commensurate with the variations shown in Ref. 32 for this magnitude of difference in magnetic moment. This suggests the difference in magnetic moment between this two sites persists despite the doping of the specimen with Si and Mn, something that may be overlooked based on the raw experimental data

In summary, by using atomic resolution EELS data of a $Mn_{0.43}Fe_{1.57}P_{0.73}Si_{0.27}$ compound, combined with an inversion technique that assumed the location of the

atomic columns in the specimen but not the Fe or Mn occupancy of each metal site, we have shown directly that the Mn atoms preferentially occupy the Fe2 sites in this compound. We also investigated the fine structure of the Fe $L_{2,3}$ edge, and found a dip in the L_3 edge on the Fe1 site, a difference that was enhanced after removing the effects of the channeling and thermal scattering of the incident electron probe, consistent with variation in magnetic moments at each atomic site.

This research was supported under the Discovery Projects funding scheme of the Australian Research Council (Project No. DP110102228). This work was sponsored by US Department of Energy, Office of Science, Basic Energy Sciences, Materials Sciences and Engineering Division and supported in part by DOE Grant No. DE-FG02-09R46554.

[1] O. Tegus, E. Brück, K. H. J. Buschow, and F. R. de Boer, Nature **415**, 150 (2002).
[2] K. A. Gschneidner Jr, V. K. Pecharsky, and A. O. Tsokol, Rep. Prog. Phys. **68**, 1479 (2005).
[3] B. G. Shen, J. R. Sun, F. X. Hu, H. W. Zhang, and Z. H. Cheng, Adv. Mater. **21**, 4545 (2009).
[4] N. H. Dung, Z. Q. Ou, L. Caron, L. Zhang, D. T. Cam Thanh, G. A. de Wijs, R. A. de Groot, K. H. Jürgen Buschow, and E. Brück, Adv. Energy Mater. **1**, 1215 (2011).
[5] N. T. Trung, Z. Q. Ou, T. J. Gortenmulder, O. Tegus, K. H. J. Buschow, and E. Brück, Appl. Phys. Lett. **94**, 102513 (2009).
[6] N. H. Dung, L. Zhang, Z. Q. Ou, and E. Brück, Scr. Mater. **67**, 975 (2012).
[7] D. T. Cam Thanh, E. Brück, N. T. Trung, J. C. P. Klaasse, K. H. J. Buschow, Z. Q. Ou, O. Tegus, and L. Caron, J. Appl. Phys. **103**, 07B318 (2008).
[8] M. Hudl, L. Häggström, E.-K. Delczeg-Czirjak, V. Höglin, M. Sahlberg, L. Vitos, O. Eriksson, P. Nordblad, and Y. Andersson, Appl. Phys. Lett. **99**, 152502 (2011).
[9] J. Sjöström, L. Häggström, and T. Sundqvist, Philos. Mag. B **57**, 737 (1988).
[10] Z. Q. Ou, L. Zhang, N. H. Dung, L. van Eijck, A. M. Mulders, M. Avdeev, N. H. van Dijk, and E. Brück, J. Magn. Magn. Mater. **340**, 80 (2013).
[11] X. B. Liu and Z. Altounian, J. Appl. Phys. **105**, 07A902 (2009).
[12] M. Bosman, V. J. Keast, J. L. García-Muñoz, A. J. D'Alfonso, S. D. Findlay, and L. J. Allen, Phys. Rev. Lett. **99**, 086102 (2007).
[13] K. Kimoto, T. Asaka, T. Nagai, M. Saito, Y. Matsui, and K. Ishizuka, Nature **450**, 702 (2007).
[14] D. A. Muller, L. F. Kourkoutis, M. Murfitt, J. H. Song, H. Y. Hwang, J. Silcox, N. Dellby, and O. L. Krivanek, Science **319**, 1073 (2008).
[15] P. Wang, A. J. D'Alfonso, S. D. Findlay, L. J. Allen, and A. L. Bleloch, Phys. Rev. Lett. **101**, 236102 (2008).
[16] M. Varela, J. Gazquez, and S. J. Pennycook, MRS Bull. **37**, 29 (2012).
[17] B. D. Forbes, A. J. D'Alfonso, R. E. A. Williams, R. Srinivasan, H. L. Fraser, D. W. McComb, B. Freitag, D. O. Klenov, and L. J. Allen, Phys. Rev. B **86**, 024108 (2012).
[18] N. R. Lugg, M. Haruta, M. J. Neish, S. D. Findlay, T. Mizoguchi, K. Kimoto, and L. J. Allen, Appl. Phys. Lett. **101**, 183112 (2012).
[19] M. G. Kanatzidis, R. Pöttgen, and W. Jeitschko, Angew. Chem. Int. Ed. **44**, 6996 (2005).
[20] P. C. Canfield and Z. Fisk, Philos. Mag. B **65**, 1117 (1992).
[21] N. W. Ashcroft and N. D. Mermin, *Solid State Physics* (Saunders College, 1976).
[22] C. Maunders, C. Dwyer, P. Tiemeijer, and J. Etheridge, Ultramicroscopy **111**, 1437 (2011).
[23] J. Verbeeck, A. Béché, and W. Van den Broek, Ultramicroscopy **120**, 35 (2012).
[24] C. Dwyer, C. Maunders, C. L. Zheng, M. Weyland, P. C. Tiemeijer, and J. Etheridge, Appl. Phys. Lett. **100**, 191915 (2012).
[25] H. L. Xin, C. Dwyer, and D. A. Muller, Ultramicroscopy **139**, 38 (2014).
[26] P. Cueva, R. Hovden, J. A. Mundy, H. L. Xin, and D. A. Muller, Microsc. Microanal. **18**, 667 (2012).
[27] N. R. Lugg, M. J. Neish, S. D. Findlay, and L. J. Allen, Microsc. Microanal. **20**, 1078 (2014).
[28] M. P. Oxley, E. C. Cosgriff, and L. J. Allen, Phys. Rev. Lett. **94**, 203906 (2005).
[29] Y. Zhu, A. Soukiassian, D. G. Schlom, D. A. Muller, and C. Dwyer, Appl. Phys. Lett. **103**, 141908 (2013).
[30] M. Varela, M. P. Oxley, W. Luo, J. Tao, M. Watanabe, A. R. Lupini, S. T. Pantelides, and S. J. Pennycook, Phys. Rev. B **79**, 085117 (2009).
[31] H. Kurata and C. Colliex, Phys. Rev. B **48**, 2102 (1993).
[32] D. M. Pease, A. Fasihuddin, M. Daniel, and J. I. Budnick, Ultramicroscopy **88**, 1 (2001).
[33] O. Eriksson, J. Sjöström, B. Johansson, L. Häggström, and H. Skriver, J. Magn. Magn. Mater. **74**, 347 (1998).